



University
of Glasgow

McCrinkle, I.J.H., Grant, J., Drysdale, T.D., and Cumming, D.R.S. (2013) Hybridization of optical plasmonics with terahertz metamaterials to create multi-spectral filters. *Optics Express*, 21 (16). pp. 19142-19152. ISSN 1094-4087

Copyright © 2013 OSA

A copy can be downloaded for personal non-commercial research or study, without prior permission or charge

The content must not be changed in any way or reproduced in any format or medium without the formal permission of the copyright holder(s)

When referring to this work, full bibliographic details must be given

<http://eprints.gla.ac.uk/85905/>

Deposited on: 23 September 2013

Enlighten – Research publications by members of the University of Glasgow
<http://eprints.gla.ac.uk>

Hybridization of optical plasmonics with terahertz metamaterials to create multi-spectral filters

Iain J. H. McCrindle, James Grant, Timothy D. Drysdale, and David R. S. Cumming*

School of Engineering, University of Glasgow, Glasgow, G12 8LT, UK

*david.cumming.2@glasgow.ac.uk

Abstract: Multi-spectral imaging systems typically require the cumbersome integration of disparate filtering materials in order to work simultaneously in multiple spectral regions. We show for the first time how a single nano-patterned metal film can be used to filter multi-spectral content from the visible, near infrared and terahertz bands by hybridizing plasmonics and metamaterials. Plasmonic structures are well-suited to the visible band owing to the resonant dielectric properties of metals, whereas metamaterials are preferable at terahertz frequencies where metal conductivity is high. We present the simulated and experimental characteristics of our new hybrid synthetic multi-spectral material filters and demonstrate the independence of the metamaterial and plasmonic responses with respect to each other.

©2013 Optical Society of America

OCIS codes: (050.6624) Subwavelength structures; (240.6680) Surface plasmons; (160.3918) Metamaterials.

References and links

1. T. May, G. Zieger, S. Anders, V. Zakosarenko, H.-G. Meyer, M. Schubert, M. Starkloff, M. Rößler, G. Thorwirth, and U. Krause, "Safe VISITOR: visible, infrared, and terahertz object recognition for security screening application," *Proc. SPIE* **7309**, 73090E (2009).
2. M. Kowalski, M. Piszczek, N. Palka, and M. Szustakowski, "Improvement of passive THz camera images," *Proc. SPIE* **8544**, 85440N, 85440N-8 (2012).
3. S. G. Kong, J. Heo, F. Boughorbel, Y. Zheng, B. R. Abidi, A. Koschan, M. Yi, and M. A. Abidi, "Multiscale fusion of visible and thermal IR images for illumination-invariant face recognition," *Int. J. Comput. Vis.* **71**(2), 215–233 (2007).
4. A. L. Chan and S. R. Schnelle, "Fusing concurrent visible and infrared videos for improved tracking performance," *Opt. Eng.* **52**(1), 017004 (2013).
5. T. W. Ebbesen, H. J. Lezec, H. F. Ghaemi, T. Thio, and P. A. Wolff, "Extraordinary optical transmission through sub-wavelength hole arrays," *Nature* **391**(6668), 667–669 (1998).
6. Q. Chen and D. R. S. Cumming, "High transmission and low color cross-talk plasmonic color filters using triangular-lattice hole arrays in aluminum films," *Opt. Express* **18**(13), 14056–14062 (2010).
7. D. Inoue, A. Miura, T. Nomura, H. Fujikawa, K. Sato, N. Ikeda, D. Tsuya, Y. Sugimoto, and Y. Koide, "Polarization independent visible color filter comprising an aluminum film with surface-plasmon enhanced transmission through a subwavelength array of holes," *Appl. Phys. Lett.* **98**(9), 093113 (2011).
8. W. J. Padilla, M. T. Aronsson, C. Highstrete, M. Lee, A. J. Taylor, and R. D. Averitt, "Electrically resonant terahertz metamaterials: theoretical and experimental investigations," *Phys. Rev. B* **75**(4), 041102 (2007).
9. H.-T. Chen, J. F. O'Hara, A. J. Taylor, R. D. Averitt, C. Highstrete, M. Lee, and W. J. Padilla, "Complementary planar terahertz metamaterials," *Opt. Express* **15**(3), 1084–1095 (2007).
10. Y.-J. Chiang, C.-S. Yang, Y.-H. Yang, C.-L. Pan, and T.-J. Yen, "An ultrabroad terahertz bandpass filter based on multiple-resonance excitation of a composite metamaterial," *Appl. Phys. Lett.* **99**(19), 191909 (2011).
11. O. Paul, R. Beigang, and M. Rahm, "Highly selective terahertz bandpass filters based on trapped mode excitation," *Opt. Express* **17**(21), 18590–18595 (2009).
12. H. P. Myers, *Introductory Solid State Physics* (CRC Press, 1997).
13. P. R. West, S. Ishii, G. V. Naik, N. K. Emani, V. M. Shalae, and A. Boltasseva, "Searching for better plasmonic materials," *Laser Photon. Rev.* **4**(6), 795–808 (2010).
14. H. F. Ghaemi, T. Thio, D. E. Grupp, T. W. Ebbesen, and H. J. Lezec, "Surface plasmons enhance optical transmission through subwavelength holes," *Phys. Rev. B* **58**(11), 6779–6782 (1998).

15. W. L. Barnes, A. Dereux, and T. W. Ebbesen, "Surface plasmon subwavelength optics," *Nature* **424**(6950), 824–830 (2003).
16. C. Genet and T. W. Ebbesen, "Light in tiny holes," *Nature* **445**(7123), 39–46 (2007).
17. J. B. Pendry, A. J. Holden, W. J. Stewart, and I. Youngs, "Extremely low frequency plasmons in metallic mesostructures," *Phys. Rev. Lett.* **76**(25), 4773–4776 (1996).
18. D. Schurig, J. J. Mock, and D. R. Smith, "Electric-field-coupled resonators for negative permittivity metamaterials," *Appl. Phys. Lett.* **88**(4), 041109 (2006).
19. Y. Ma, A. Khalid, T. D. Drysdale, and D. R. S. Cumming, "Direct fabrication of terahertz optical devices on low-absorption polymer substrates," *Opt. Lett.* **34**(10), 1555–1557 (2009).
20. A. M. Melo, M. A. Kornberg, P. Kaufmann, M. H. Piazzetta, E. C. Bortolucci, M. B. Zakia, O. H. Bauer, A. Poglitsch, and A. M. da Silva, "Metal mesh resonant filters for terahertz frequencies," *Appl. Opt.* **47**(32), 6064–6069 (2008).
21. J. B. Pendry, "Negative refraction makes a perfect lens," *Phys. Rev. Lett.* **85**(18), 3966–3969 (2000).
22. L. Lin, X. M. Goh, L. P. McGuinness, and A. Roberts, "Plasmonic lenses formed by two-dimensional nanometric cross-shaped aperture arrays for fresnel-region focusing," *Nano Lett.* **10**(5), 1936–1940 (2010).
23. Q. Chen and D. R. S. Cumming, "Visible light focusing demonstrated by plasmonic lenses based on nano-slits in an aluminum film," *Opt. Express* **18**(14), 14788–14793 (2010).
24. L. Verslegers, P. B. Catrysse, Z. Yu, J. S. White, E. S. Barnard, M. L. Brongersma, and S. Fan, "Planar lenses based on nanoscale slit arrays in a metallic film," *Nano Lett.* **9**(1), 235–238 (2009).
25. J. B. Pendry, D. Schurig, and D. R. Smith, "Controlling electromagnetic fields," *Science* **312**(5781), 1780–1782 (2006).
26. U. Leonhardt, "Optical conformal mapping," *Science* **312**(5781), 1777–1780 (2006).
27. N. I. Landy, S. Sajuyigbe, J. J. Mock, D. R. Smith, and W. J. Padilla, "Perfect metamaterial absorber," *Phys. Rev. Lett.* **100**(20), 207402 (2008).
28. H. Tao, N. I. Landy, C. M. Bingham, X. Zhang, R. D. Averitt, and W. J. Padilla, "A metamaterial absorber for the terahertz regime: design, fabrication and characterization," *Opt. Express* **16**(10), 7181–7188 (2008).
29. J. Grant, Y. Ma, S. Saha, L. B. Lok, A. Khalid, and D. R. S. Cumming, "Polarization insensitive terahertz metamaterial absorber," *Opt. Lett.* **36**(8), 1524–1526 (2011).
30. J. Grant, Y. Ma, S. Saha, A. Khalid, and D. R. S. Cumming, "Polarization insensitive, broadband terahertz metamaterial absorber," *Opt. Lett.* **36**(17), 3476–3478 (2011).
31. P. B. Catrysse and B. A. Wandell, "Integrated color pixels in 0.18- μm complementary metal oxide semiconductor technology," *J. Opt. Soc. Am. A* **20**(12), 2293–2306 (2003).
32. Q. Chen, D. Chitnis, K. Walls, T. D. Drysdale, S. Collins, and D. R. S. Cumming, "CMOS photodetectors integrated with plasmonic color filters," *IEEE Photon. Technol. Lett.* **24**(3), 197–199 (2012).
33. Q. Chen, D. Das, D. Chitnis, K. Walls, T. D. Drysdale, S. Collins, and D. R. S. Cumming, "A CMOS image sensor integrated with plasmonic colour filters," *Plasmonics* **7**(4), 695–699 (2012).
34. A. W. M. Lee, B. S. Williams, S. Kumar, Q. Hu, and J. L. Reno, "Real-time imaging using a 4.3-THz quantum cascade laser and a 320x240 microbolometer focal-plane array," *IEEE Photon. Technol. Lett.* **18**(13), 1415–1417 (2006).
35. B.-Y. Hsieh and M. Jarrahi, "Analysis of periodic metallic nano-slits for efficient interaction of terahertz and optical waves at nano-scale dimensions," *J. Appl. Phys.* **109**(8), 084326 (2011).
36. C. M. Bingham, H. Tao, X. Liu, R. D. Averitt, X. Zhang, and W. J. Padilla, "Planar wallpaper group metamaterials for novel terahertz applications," *Opt. Express* **16**(23), 18565–18575 (2008).
37. R. P. Feynman, R. B. Leighton, and M. L. Sands, *The Feynman Lectures on Physics* (Addison-Wesley, 1977, (II)).
38. N. Laman and D. Grischkowsky, "Terahertz conductivity of thin metal films," *Appl. Phys. Lett.* **93**(5), 051105 (2008).
39. A. D. Rakić, "Algorithm for the determination of intrinsic optical constants of metal films: application to aluminum," *Appl. Opt.* **34**(22), 4755–4767 (1995).
40. M. Naftaly and R. E. Miles, "Terahertz time-domain spectroscopy of silicate glasses and the relationship to material properties," *J. Appl. Phys.* **102**(4), 043517 (2007).
41. J. B. Pendry, L. Martín-Moreno, and F. J. Garcia-Vidal, "Mimicking surface plasmons with structured surfaces," *Science* **305**(5685), 847–848 (2004).
42. J. B. Pendry, A. J. Holden, D. J. Robbins, and W. J. Stewart, "Magnetism from conductors and enhanced nonlinear phenomena," *IEEE Trans. Microw. Theory Tech.* **47**(11), 2075–2084 (1999).
43. D. R. Smith, W. J. Padilla, D. C. Vier, S. C. Nemat-Nasser, and S. Schultz, "Composite medium with simultaneously negative permeability and permittivity," *Phys. Rev. Lett.* **84**(18), 4184–4187 (2000).
44. D. R. Smith, D. C. Vier, Th. Koschny, and C. M. Soukoulis, "Electromagnetic parameter retrieval from inhomogeneous metamaterials," *Phys. Rev. E Stat. Nonlin. Soft Matter Phys.* **71**(3 3 Pt 2B), 036617 (2005).
45. Lumerical finite difference time domain (FDTD) Solutions. <http://www.lumerical.com>
46. E. D. Palik, *Handbook of Optical Constants of Solids* (Elsevier Science & Tech, 1985), (I, II, III).
47. F. A. Jenkins and H. E. White, *Fundamentals of Optics* (McGraw-Hill, 1981).

1. Introduction

Multi-spectral imaging exploits different contrast mechanisms and data-fusion in order to extract more information from a scene than is available in any single spectral band alone [1–4]. Imaging technology uses different materials, suitable to the wavelength of operation to make band selective imagers. For example, a digital camera uses dyed polymer filters fabricated on to a complementary metal-oxide-semiconductor (CMOS) chip to record separately the red, green and blue color bands, whereas interference filters are widely used in the infrared (IR). Traditional techniques impose undesirable restrictions on multi-spectral imaging systems because different filtering materials do not lend themselves well to co-integration. We propose an alternative approach using a structured material that exploits multiple modes of operation thus opening up the possibility of multiband imagers suitable for large spectral ranges. Candidate technologies include the use of nanolithography to make color filters using surface plasmon resonance (SPR) [5–7], and metamaterials (MM) to filter terahertz radiation [8–11].

In order to understand how these different modalities can be combined, it is important to consider the electromagnetic properties of the constituent materials from which the structures will be made. The electromagnetic properties of a material may be described in terms of the dielectric function, ϵ . The Drude model describes ϵ , which is resonant in character, and contains a quantity known as the plasma frequency, ω_p . For metals, ω_p typically occurs at the ultraviolet (UV) region of the spectrum, yielding a negative dielectric constant from near UV to lower frequencies [12, 13]. The resulting resonant characteristic is frequently described in terms of surface plasmons (SPs) that are electron density oscillations at a metal-dielectric interface [12]. The physical process underlying plasmonics is SPR wherein incident light resonantly couples with SPs to form surface plasmon polaritons (SPPs) [5, 14–16]. Ebbesen *et al.* reported on the transmission of light through a silver film patterned with a periodic array of subwavelength holes as a consequence of SPR [5].

Plasmonics typically act in metal at visible and IR wavelengths, however at lower frequencies, towards the far infrared (FIR), or the terahertz, region of the spectrum, the loss component of the permittivity dominates since the metal is a conductor [13, 17]. However, metal can still be structured to elicit an electromagnetic response by fabricating electric ring resonators (ERR). These structures have resonant characteristics that rely on current flow driven by the incident electric field. ERRs are MM unit cells that can be formed into an array that displays an effective permittivity, ϵ_{eff} , as though it was a bulk material [8, 9, 18]. Metal-based MMs, ERR-like structures and plasmonics have been used to design many devices including filters [6, 7, 10, 11, 19, 20], lenses [21–24], invisibility cloaks [25, 26] and perfect absorbers [27–30].

Our synthetic multi-spectral material (SMM) juxtaposes the distinct features of a MM filter with plasmonic filters. In this article we design and fabricate a SMM that selectively filters light in the visible, near infrared (NIR) and terahertz bands in a single aluminum film and can be integrated with the dominant imaging technology (CMOS) to create a multi-spectral imaging system capable of simultaneous color imaging [31–33] and frequency selective terahertz imaging [34] that operates in a manner similar to the standard digital camera. This improves on previous theoretical studies that suggest periodic metallic slit arrays can support two passbands simultaneously [35].

2. Simulation of plasmonic and metamaterial structures

The SMM uses specific structural and compositional parameters to ensure that the optical and terahertz resonances can occur simultaneously whilst having minimal impact on each other. Plasmonic filters are strongly affected by metal type, metal thickness, surrounding dielectric media, and the hole array pattern [14–16], whereas MM filter performance is most greatly impacted by the overall geometry of the MM structure [8, 9, 36]. These features make

it possible to design SMM structures in which the optical properties in different regions of the spectrum are independently tuned.

Plasmonic filtering has been demonstrated with hole arrays patterned onto a 150 nm aluminum film [6, 7]. Typically silver and gold have been used for plasmonic applications; however aluminum is low cost, easy to fabricate and is CMOS compatible. The skin depth of aluminum, δ , at 2 THz is less than 60 nm [37–39] therefore a 150 nm aluminum film is also a suitable material for a terahertz MM filter. Using this information we can see that it is possible to pattern both of these structures into a single 150 nm aluminum layer to create a SMM.

The aluminum should ideally be fabricated on top of a dielectric surface to maintain mechanical stability. Since plasmonic filters require index matching between top and bottom layers to optimize performance, a dielectric cap layer must also be present [6]. Silicon dioxide is suitable for color plasmonics since it exhibits low loss at optical wavelengths, however it has a higher absorption coefficient, α , at terahertz frequencies. It has previously been reported that $\alpha = 780 \text{ m}^{-1}$ at 2 THz [40], therefore, a significant amount of terahertz radiation will be absorbed in a silicon dioxide substrate that has a thickness of several hundred microns, but a thin membrane will be adequately transparent.

Our SMM layer structure takes advantage of these properties of aluminum and silicon dioxide. To minimize the loss of transmitted terahertz radiation we used a 3 μm silicon dioxide membrane, a 150 nm aluminum film patterned with plasmonic and MM structures, and a 200 nm cap layer to index match the surfaces above and below the aluminum.

A triangular hole array is preferable to the more conventional square array for plasmonic filters because the triangular periodic structure yields a larger gap between adjacent transmission peaks, which is desirable for wavelength discrimination [6, 15, 16]. The resonant wavelength of the normal incidence transmission spectra for a triangular hole array can be approximated by the following dispersion relation:

$$\lambda_{max} = \frac{P}{\sqrt{\frac{4}{3}(i^2 + ij + j^2)}} \sqrt{\frac{\epsilon_m \epsilon_d}{\epsilon_m + \epsilon_d}}. \quad (1)$$

where λ_{max} is the resonant wavelength, P is the period of the hole array, ϵ_m and ϵ_d are the permittivities of the metal and dielectric, respectively, and i and j are the scattering orders [6, 16]. The triangular array and the corresponding unit cell are shown in Fig. 1(a), where P denotes the array period.

An ERR can be used to make a band-reject MM filter [8]. Alternatively, a complementary ERR (cERR) structure yields a complementary band-pass electromagnetic response, consistent with Babinet's principle [9]. We exploited this concept to design a MM filter consisting of an array of cERRs based on a hollow cross ERR design [29]. Similar MM filter structures have been shown to operate at terahertz frequencies [10, 11], and have the desirable property that we can maximize the MM metal area available for patterning to make the SPR filters.

Typically an optical material is described by its dielectric function. As described above a metal SPR may be described by the Drude resonance model. In order to show the multi-resonance characteristics of the SMM we extract the effective dielectric function for the MM. The effective medium description of the MM leads to the concept of spoof SPs which are electromagnetic surface modes due to subwavelength structures in the metal. At terahertz frequencies, where real SPs cannot be supported because of the high conductivity of the metal, spoof SPs play an analogous role to real SPs. At resonance, spoof SPs have been proposed as the cause of enhanced transmission [41].

MMs are typically described in terms of their complex effective electromagnetic parameters, namely the refractive index, n_{eff} , the wave impedance, z_{eff} , the electric

permittivity, ϵ_{eff} , and the magnetic permeability, μ_{eff} [17, 27, 42, 43]. The effective electromagnetic parameters are calculated using scattering parameters determined by simulation results, and the following equations:

$$n_{eff} = \frac{1}{kd} \cos^{-1} \left[\frac{1}{2S_{21}} (1 - S_{11}^2 + S_{21}^2) \right]. \quad (2)$$

$$z_{eff} = \sqrt{\frac{(1 + S_{11})^2 - S_{21}^2}{(1 - S_{11})^2 - S_{21}^2}}. \quad (3)$$

$$\epsilon_{eff} = \frac{n_{eff}}{z_{eff}}. \quad (4)$$

$$\mu_{eff} = n_{eff} z_{eff}. \quad (5)$$

where k is the wavenumber of the incident light, d is the thickness of the MM and S_{21} and S_{11} are the complex transmission and reflection scattering parameters, respectively, after having been corrected for the phase shift that is observed due to the reduced wavelength of the plane wave in the dielectric medium [44].

The SMM was designed and optimized using Lumerical's finite difference time domain (FDTD) tool [45]. A 3D simulation model was used throughout to investigate the behavior of the SMM in visible to NIR (400 nm to 1 μ m) and terahertz (1 THz to 9 THz) wavelength regimes.

2.1 Nanoholes at terahertz frequencies

The wavelength of radiation in the terahertz region and the period of the MM structures are much larger than our visible and NIR plasmonic structures, so that a simulation of the subwavelength holes in a complete SMM structure was found to be particularly memory intensive and therefore impractical. To overcome this problem, an investigation into how the presence of nanoholes in a metal film affects the transmission and reflection of incident terahertz radiation was carried out.

An aluminum film, defined by complex refractive index parameters [39], was positioned on the x - y plane. The film was perforated by a single nanohole with a diameter of 140 nm. Anti-symmetric and symmetric boundary conditions were used in x and y , respectively, to form a square hole array with a period of 250 nm. The z boundaries used perfectly matched layers. A uniform mesh was used in the region of the metal with maximum cell sizes of $\Delta x = \Delta y = \Delta z = 5$ nm. The aluminum film was illuminated normally by a terahertz plane wave source and the resultant transmission and reflection spectra were recorded at 1 THz to 9 THz. Simulations were performed for aluminum thicknesses ranging from 50 nm to 200 nm and also repeated for films without nanoholes. In all simulations, the transmission did not exceed 3.3×10^{-5} and was of the order of 10^{-6} for a 150 nm aluminum film patterned with holes. It is therefore reasonable to describe an aluminum plasmonic filter at terahertz frequencies as an optically thick metal film without perforations. These results are also in agreement with our understanding that the aluminum skin depth is small at terahertz frequencies, as discussed previously [38, 39].

The simulations were repeated for triangular hole arrays in a 150 nm aluminum film with periods of 230 nm and 550 nm, and hole diameters of 130 nm and 290 nm, respectively. These parameters correspond to blue and NIR filters and transmission was once again observed to be of the order of 10^{-6} . The minimal impact on transmission of terahertz radiation through a 150 nm aluminum film with nanohole perforations means that it is

possible to simulate the plasmonic filters and MM filter structures independently to investigate the filtering characteristics of the SMM at optical and terahertz wavelengths.

2.2 Plasmonic filter simulation

The simulation was set up as previously described, however in this case, the aluminum was sandwiched between a semi-infinite silicon dioxide superstrate and a 200 nm silicon dioxide cap layer. Lumerical's default material database holds Palik aluminum and silicon dioxide models that were used to define the constituent materials of the filters at optical wavelengths [46]. The aluminum was patterned with a triangular array of 150 nm deep silicon dioxide cylinders and the silicon dioxide cap layer was patterned with corresponding 150 nm air cylinders, to account for the aluminum resulting in a non-uniform cap layer after fabrication. The period and hole size of the arrays were varied and optimized for each of sixteen filters to yield discrete wavelength filtering in the visible and NIR band. A plane wave source ranging from 400 nm to 1 μm was perpendicularly incident on the top surface of the aluminum film and a transmission monitor was positioned at a distance of 800 nm from the silicon dioxide cap layer.

2.3 Metamaterial filter simulation

It was necessary to find the optimum cERR geometry that maximizes the metal area available to be patterned with nanoholes without compromising significantly on terahertz filtering characteristics. The MM filter was simulated using a 150 nm aluminum film, defined by complex refractive index parameters at terahertz frequencies [39], sandwiched between a 3 μm silicon dioxide layer and 200 nm silicon dioxide layer. Silicon dioxide, again, used Palik refractive index model from the Lumerical database [46]. The structure was positioned in the x - y plane. A 150 nm silicon dioxide etched cross was placed in the aluminum layer, thereby forming the unit cell as seen in Fig. 1(b). A modified version of Lumerical's S-parameter extraction analysis script was used to post-process simulation data. Transmission and reflection monitors were placed at distances 247 μm and 250 μm from the MM, respectively. Refractive index monitors were also used at these positions as this data was required to carry out phase correction on the scattering parameters. A terahertz plane wave source was incident perpendicularly onto the cERR surface. The unit cell was repeated by using anti-symmetric and symmetric boundary conditions in x and y , respectively, and perfectly matched layers were used in z . The maximum mesh steps through the cross structure were $\Delta x = \Delta y = 75$ nm and $\Delta z = 25$ nm.

In other work we explored an empty cross filter structure [19]. It was found that for a given unit-cell size, the resonant wavelength of the in-filled cERR we have investigated in this work, was approximately doubled compared to the empty cross.

3. Design and fabrication of the synthetic multi-spectral material

After separately optimizing the plasmonic filter and MM filter structures, we combined them into a single SMM design. In addition to the influence of the substrate the terahertz transmission magnitude also depends on the metal fill factor of the cERR. A high metal fill factor is desirable because it maximizes the area available for implementing the plasmonic filters, but this had to be balanced against an accompanying reduction in the transmission magnitude and decrease in bandwidth, as determined by simulations.

A unit cell of the cERR structure used in the SMM is shown in Fig. 1(b) and the dimensions of the cERR are as follows: $A = 21$ μm , $B = 6$ μm , $C = 8$ μm , $D = 23$ μm with a periodicity of 27 μm . The metal regions of the cERR were patterned with triangular hole arrays of varying sizes and periods to act as a plasmonic filter set. An illustration of the patterned aluminum film of the SMM at varying length scales is shown in Fig. 1(c). On the metal surface the cERR array extends to an area of 12 mm x 12 mm. Within this area we placed sixteen plasmonic filters, each 1 mm x 1 mm in size and separated from the next

adjacent filter by 0.33 mm. A cross-section of the fabricated SMM structure is shown in Fig. 1(d).

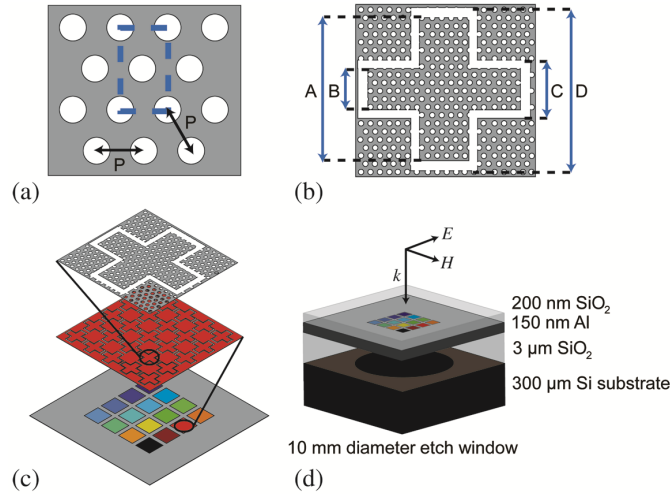


Fig. 1. Synthetic multi-spectral material (SMM) schematic. (a) Schematic of a plasmonic filter with unit cell highlighted and the array period, P , shown. (b) Schematic of a terahertz metamaterial (MM) filter unit cell with complementary electric ring resonator (cERR) dimensions shown. A plasmonic hole array is included, however it is not to scale. (c) An illustration of the SMM at various length scales. (d) A cross section of the SMM showing the layer structure and incident field direction shown by propagation vector, k .

The structure was built up on a silicon substrate, then a circular window with a 10 mm diameter was back-side etched through the silicon to the silicon dioxide membrane. The first step in fabricating the SMM was to deposit a 3 μm layer of silicon dioxide on to a clean piece of silicon. A 150 nm aluminum film was evaporated on to the silicon dioxide surface and an additional 50 nm layer of silicon nitride was then deposited on to the aluminum surface to assist with adhesion of the electron beam resist. ZEP520A was spin coated on to the silicon nitride surface and holes were defined in the electron beam resist using a Vistec VB6 electron beam lithography (EBL) tool. The pattern was developed using *o*-xylene, and the silicon nitride and aluminum holes were etched using trifluoromethane / oxygen ($\text{CHF}_3 / \text{O}_2$) in a Oxford Instruments RIE80 + dry etch tool and silicon tetrachloride (SiCl_4) in a Oxford Instruments RIE100 dry etch tool, respectively. The remaining resist and silicon nitride were removed and the sample was cleaned. At this stage, a scanning electron microscope (SEM) was used to investigate the quality of the etched holes. Finally, a 200 nm silicon dioxide cap layer was deposited on to the aluminum surface. To complete the device it was necessary to back etch the silicon substrate to open a window for optical and terahertz transmission measurements. The silicon dioxide cap layer was spin coated with S1818 photoresist to act as a protective coating for subsequent processing. The silicon surface was then spin coated with AZ4562 photoresist and a 10 mm diameter circle was exposed using a photomask and Suss MA6 optical mask aligner. The window was developed using diluted AZ400K developer and the device was then placed on a carrier wafer before being etched using a STS ICP RIE. Figure 2 shows images of the experimental structure with a SEM image of the SMM surface, consisting of an etched cERR and nanoholes in Fig. 2(a); a SEM image of a plasmonic filter in Fig. 2(b); and transmission optical microscope images of the SMM over different plasmonic filter regions in Figs. 2(c)-2(f).

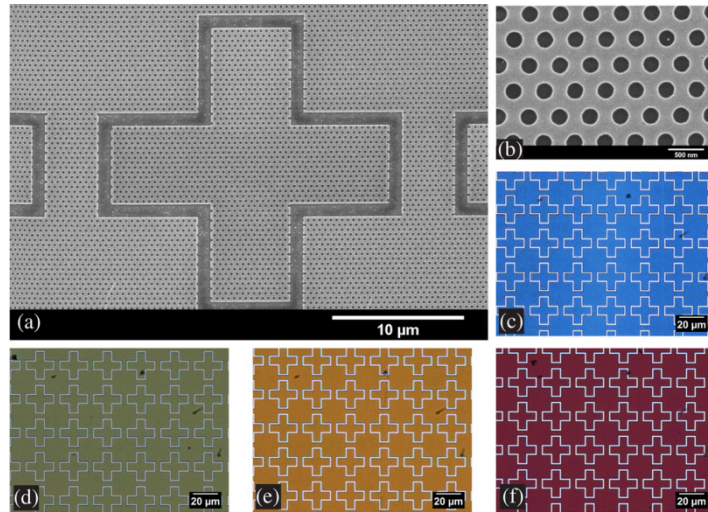


Fig. 2. Images of a fabricated synthetic multi-spectral material (SMM). (a) A scanning electron micrograph of the etched complementary electric ring resonator (cERR) structure and hole array (period 430 nm). (b) A scanning electron micrograph of the etched hole array (period 430 nm) on the metal film. (c) Transmission microscope images of the SMM showing blue (hole period 250 nm), (d) green (hole period 340 nm), (e) yellow (hole period 380 nm) and (f) red (hole period 430 nm) plasmonic filters with the cERR array.

4. Experimental characterization of the synthetic multi-spectral material

The transmission spectra from each of the sixteen plasmonic filter regions of the SMM were measured with a TFProbe MSP300 microspectrophotometer. Unpolarized white light from a halogen lamp was transmitted through the sample and collected by a camera with a detector spot size of 100 μm . A white light background spectrum was taken as a reference measurement.

A Bruker IFS 66v/S Fourier transform infrared spectrometer (FTIR) was used to characterize the terahertz filtering capabilities of the SMM. The terahertz source was a mercury arc lamp with a 12 mm diameter source aperture. A background spectrum was measured by placing a mask with a 7 mm diameter circular window between the source and the detector. The SMM was then attached to the mask and the filtered spectrum was measured and normalized to the background spectrum. The filtering characteristics of the SMM are shown in Fig. 3.

Fabry-Perot oscillations are present in the color filter transmission spectra due to the silicon dioxide membrane acting as a 3 μm cavity [47]. The oscillation peaks are slightly shifted across the various plasmonic filters owing to a slight bowing of the membrane due to stress.

The plasmonic filter simulations were repeated using hole sizes that had been measured with SEM images of the fabricated filter array, as listed in Fig. 3, so as to fully account for the geometry of the as-fabricated devices. The simulated peak wavelengths and experimentally measured peak wavelengths from the SMM for the sixteen different array periods are shown in Fig. 4(a) and can be seen to exhibit a linear relationship, in agreement with Eq. (1). The apparent plateaus in the experimental data (e.g. $330\text{nm} \leq P \leq 350\text{ nm}$) arise from the Fabry-Perot resonances.

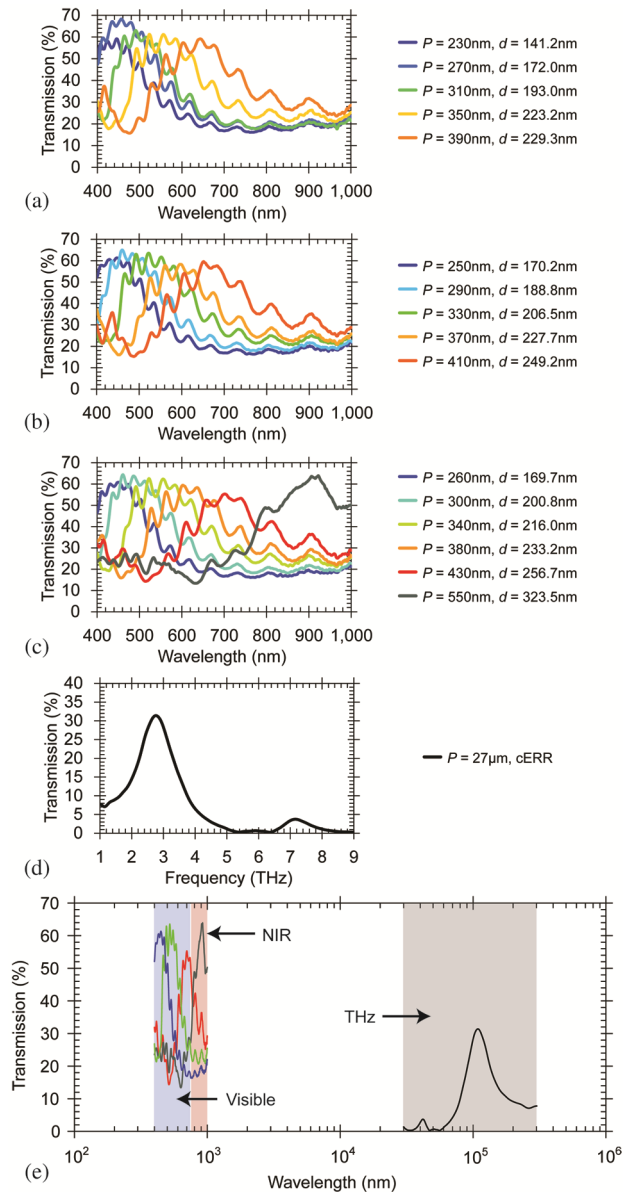


Fig. 3. Measured transmission spectra for the synthetic multi-spectral material (SMM). The individual filter spectra are shown in (a)-(d). The legend denotes the hole period, P , and diameter, d , for the plasmonic filters. cERR denotes the spectral characteristics due to the metamaterial (MM) filter component. (e) SMM spectral characteristics over a large wavelength range. Plasmonic filter regions of the SMM with hole periods: 250 nm (blue), 330 nm (green), 430 nm (red) and 550 nm (near infrared) are shown in addition to the MM filter component.

There is no visible light resonant response associated with the cERRs and the plasmonic nanoholes are sufficiently subwavelength compared with FIR radiation that they do not influence the terahertz response of the device. However, the cERR gaps result in some white light transmission across the measured spectrum in addition to the plasmonic color filtering. An approximation of the standalone plasmonic filter spectra, that would be observed if the

cERR gaps were not present, is acquired by considering the metal fill factor (88% of the surface area) and scaling the measured spectra accordingly.

The simulated transmission spectra and the scaled experimentally measured transmission spectra from the SMM for red, green and blue (RGB) filters are shown in Fig. 4(b). The simulated structure did not include a 3 μm silicon dioxide layer and therefore no Fabry-Perot modes are observed in the simulated spectra. Other than the expected absence of Fabry-Perot oscillations, there is good agreement between the simulated spectra and the scaled measured spectra. The effect of the cERR gaps could be reduced and possibly eliminated for specific applications, such as CMOS imaging, by careful consideration of the cERR positioning and geometry.

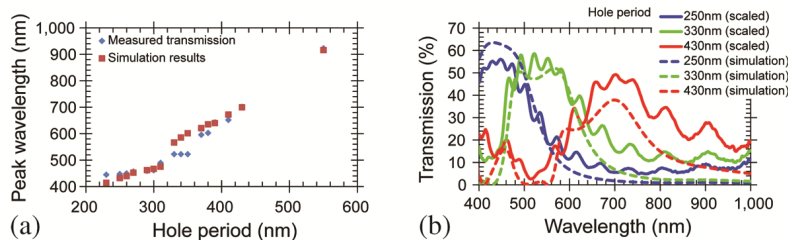


Fig. 4. Comparison of the simulated standalone plasmonic filter spectra and the measured transmission spectra of plasmonic filter regions of the synthetic multi-spectral material (SMM). (a) A comparison of simulated peak wavelength with experimentally measured peak wavelength for the sixteen plasmonic filters included on the SMM. (b) Simulated transmission spectra for standalone RGB plasmonic filters and the scaled SMM RGB plasmonic filter spectra. The SMM spectra are scaled to account for the presence of the complementary electric ring resonator (cERR) gaps.

In addition to the visible and NIR filtering characteristics, the device also exhibits a transmission peak of 31% at 2.75 THz due to the MM filter structure. These experimental results clearly demonstrate the large wavelength range over which we can control the bandpass characteristics of a single metal film by exploiting plasmonic and MM phenomena simultaneously.

We refined our MM filter simulations to account for the properties of the materials as deposited in fabrication. The aluminum was modeled using the same refractive index parameters as had been used previously for terahertz frequencies [39] and the silicon dioxide refractive index was chosen to be $n = 1.68 + i0.16$. This suggests that the silicon dioxide we have deposited has a higher absorption coefficient and different refractive index than has been reported for silicon dioxide previously [40]. Our simulated transmission spectrum yields a magnitude of 37% and peak frequency of 2.65 THz, which is in good agreement with the experimentally observed spectrum of the SMM which has a peak at 2.75 THz of 31% as is shown in Fig. 5(a). Also included for comparison is the measured transmission spectrum from a standalone MM filter with the same cERR design, but lacking the plasmonic structures. The standalone terahertz filter exhibits a transmission peak of 34% at 2.74 THz. These results demonstrate that the terahertz filtering capabilities are only slightly modified by the presence of the plasmonic filters.

In our characterization experiments and simulations the terahertz radiation is perpendicularly incident on the surface of the MM; the magnetic field is incapable of inducing currents within the material and the resonant response is due only to the electric field driving currents on the metal surface. The surface currents and the cERR geometry lead to inductive and capacitive effects, resulting in electric field enhancement and transmission of a discrete frequency band [8, 9, 11]. Using Eqs. (2)-(5) we have extracted the effective MM parameters. The lack of a magnetic response in the MM is observed in the extracted permeability (not shown) where, in the effective medium limit, its real and imaginary

components are approximately one and zero, respectively. Our device can therefore be classed as an electrically resonant MM and the observed phenomena can be described in terms of the extracted effective permittivity as shown in Fig. 5(b). Also shown for comparison is the complex permittivity of bulk aluminum at UV wavelengths [39]. In this region the permittivity crosses zero and we observe the plasma frequency of aluminum. For our MM filter the real part of the effective permittivity crosses zero at the resonant frequency, which can be considered an effective plasma frequency, analogous to the plasma frequency observed in aluminum at UV wavelengths. The imaginary component of the effective permittivity is small in the region of the resonance. These features show a characteristic effective Drude response, as is typical of this type of MM filter [9, 11].

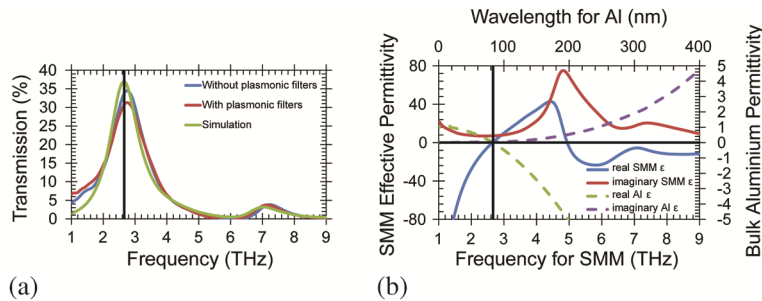


Fig. 5. Metamaterial (MM) filter simulation results and extracted effective parameters. (a) Simulated transmission spectra. The experimental results of the synthetic multi-spectral material (SMM) filter and a standalone MM filter without plasmonic filters are shown for comparison. (b) The complex effective permittivity of the SMM at terahertz frequencies and bulk aluminum permittivity at UV wavelengths. The vertical line denotes where the real effective permittivity of the SMM and the real permittivity of bulk aluminum crosses zero. This is at the effective plasma frequency of the SMM and the plasma frequency of aluminum. The bottom x axis and the left y axis are for the SMM effective parameters. The top x axis and the right y axis are for aluminum parameters.

5. Conclusion

In this article we have shown the successful hybridization of two optical technologies: a MM filter and plasmonic filters, to create a new type of synthetic multi-spectral material. The resulting device is capable of simultaneously filtering terahertz, NIR and visible radiation, thereby eliminating the requirement for multiple optical components to achieve these purposes. It has been demonstrated experimentally and by simulation that the presence of plasmonic filters on a MM filter have a negligible impact on its responsivity and that plasmonic filtering of optical wavelengths are unaffected by a cERR layer, other than by an expected increase in transmission intensity. Modification of the cERR layer for specific purposes can ensure that this effect is minimized and possibly eliminated.

This new material demonstrates that the optical passband characteristics of a thin film can be engineered over several decades of wavelength using a single lithographic step. It ensures that the spectral information acquired per unit area is maximized and can therefore be used to make high resolution, multipurpose detectors.

Acknowledgments

The authors would like to thank the staff of the James Watt Nanofabrication Centre at the University of Glasgow for help in fabricating the devices reported in this paper. This research was funded from EPSRC grants EP/I017461/1 and EP/J018678/1.